J. Fluid Mech. (2006), *vol.* 569, *pp.* 1–28.
doi:10.1017/S0022112006001911 Printed in the United Kingdom

Azimuthal vorticity gradient in the formative stages of vortex breakdown

By M. KUROSAKA[1]†, C. B. CAIN[1], S. SRIGRAROM[1], J. D. WIMER[1], D. DABIRI[1], W. F. JOHNSON III[1], J. C. HATCHER[1], B. R. THOMPSON[1], M. KIKUCHI[2], K. HIRANO[2], T. YUGÉ[2] AND T. HONDA[2]

[1]Department of Aeronautics and Astronautics, University of Washington, Seattle, WA 98195-2400, USA
[2]Mechanical System Engineering, Miyazaki University, Miyazaki, Japan

(Received 8 February 2005 and in revised form 13 February 2006)

This paper is motivated by an observation: in the nascent state of vortex breakdown before it develops into a full-grown radial expansion, an initially straight vortex core first swells, and does so even in a straight pipe for no apparent reason. Although this initial swelling may be explained in many ways according to the perspectives chosen, we offer our own interpretation framed solely within vorticity dynamics: the radial swelling as well as the subsequent growth are induced by the azimuthal vorticity gradient decreasing downstream. The negative azimuthal vorticity gradient first appears at start-up and moves eventually into the region where the circulation reaches its steady-state value. The vorticity gradient can become negative without necessarily being accompanied by a sign-switch of the azimuthal vorticity itself.

The key point – that the negative azimuthal vorticity gradient induces initial radial swelling and its growth – is demonstrated in two analyses. First, a kinematic analysis results in an equation for the radial velocity where the azimuthal vorticity gradient appears as a source term. Its solution shows, in general and explicitly, that the negative azimuthal vorticity gradient does induce radially outward velocity. Two heuristic examples serve to illustrate this point further. In the second analysis, using the equation of motion in the streamline coordinates, the negative azimuthal vorticity gradient is shown to diverge the meridional streamlines radially. A numerical simulation using a modified vortex filament method not only corroborates this role of the azimuthal vorticity gradient in initiating and promoting the radial expansion, but also adds details to track the formation process. Both analyses and simulation support our interpretation that the initial radial swelling and its subsequent growth are induced by the negative azimuthal vorticity gradient.

1. Introduction

The phenomenon of vortex breakdown is of intriguing complexity, and can be interpreted and understood in many different ways. A legion of definitive experiments, ingenious theories and illuminating numerical simulations have been put forth by various authors, which have enriched our understanding of the phenomenon (e.g. Benjamin 1962; Sarpkaya 1971; Garbowski & Berger 1976; Escudier, Bornstein & Maxworthy 1982; Spall, Gatski & Ash 1990; Brown & Lopez 1990; Beran & Culick

† Author to whom correspondence should be addressed: kurosaka@aa.washington.edu.

1992; Leibovich & Kribus 1990; Buntine & Saffman 1995; Visbal 1996; Goldshtik & Hussain 1997; Saghbini & Ghoniem 1997; Wang & Rusak 1997; Darmofal *et al.* 2001; Ruith *et al.* 2003). Since in this limited space we cannot discuss these and other important papers, we refer to review articles by Leibovich (1984), Delery (1994), and Lucco-Negro & O'Doherty (2001).

Here, with a focus upon the transient formative stage of vortex breakdown, we consider a simple question: "For an initially straight vortex core, what initiates its radial expansion?"

This initial radial enlargement has often been attributed to an adverse pressure gradient: for instance, in a swirling pipe flow, an increase of pressure in the divergent section of the pipe. But even in a straight pipe, vortex breakdowns are known to occur (e.g. Bellamy-Knights 1976; Kurosaka *et al.* 2003). In view of the overall pressure drop through the pipe, what then triggers the enlargement of the otherwise straight vortex core?

Although other explanations for this initial radial bulge may be offered, our interpretation based on vorticity dynamics is this: it is caused by the self-induction by the azimuthal vorticity decreasing downstream or negative gradient of the azimuthal vorticity, which appears first in the start-up.

For a steady and fully developed state of vortex breakdown, Brown & Lopez (1990) demonstrated the direct connection between the sign-switch in the azimuthal vorticity and the radial expansion. However, even in the absence of the sign-switch, it is the negative gradient of the azimuthal vorticity that triggers the initial radial swelling and sustains its subsequent growth. The sign-switch of the azimuthal vorticity itself may be regarded as a special case of the negative azimuthal vorticity gradient; when the upstream positive azimuthal vorticity changes to negative downstream, its gradient becomes negative. But the negative azimuthal vorticity can exist even when the azimuthal vorticity does not switch its sign. This crucial role of the negative gradient of the azimuthal vorticity does not seem to have received the attention it warrants.

We start with the observed transient flow preceding the vortex breakdown and describe how, in such an early transient stage, the negative azimuthal vorticity gradient may originate.

2. Transient formation and generation of the azimuthal vorticity gradient

As an early sign of vortex breakdown, an initially straight vortex core reveals a hint of an impending change, a slight swelling, an example of which is shown in figure 1.

It was obtained in a straight pipe fitted with upstream guide vanes in a test rig at Miyazaki University. Its original setup is described in Kurosaka *et al.* (2003). Figure 1 was obtained by installing a quick activating valve downstream of the test section, which was opened suddenly to achieve impulsive transient formation of vortex breakdown; the opening of the guide vanes was fixed. The initially straight dye starts to swell at 5 s after the opening of the valve (figure 1*b*), followed by the continuous radial enlargement into a bubble, which maintains near symmetry up to 7.83 (figure 1*f*), until asymmetry starts to develop downstream.

Though not visible in figure 1 for the centerline, dyes injected slightly off-centre display spiralling vortical structure (e.g. Srigrarom 2001), as displayed in figure 2 (Srigrarom 2001) for a delta wing at 20° of angle-of-attack when the free-stream velocity was quickly increased.

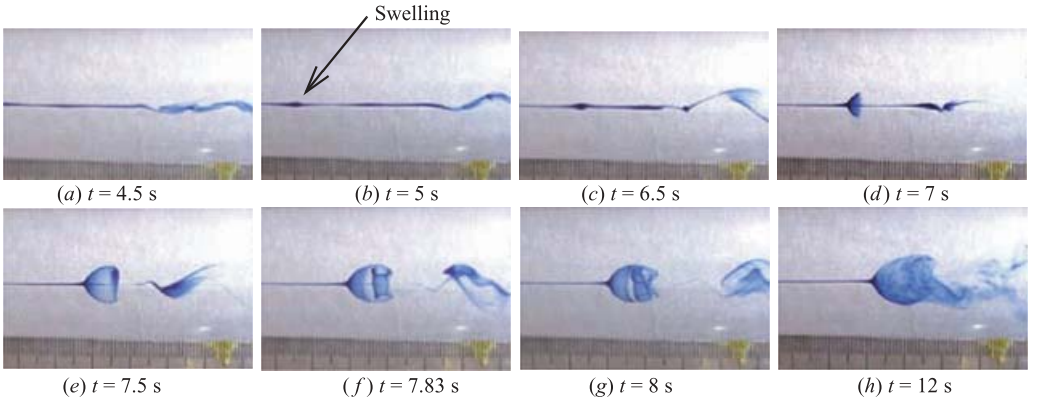

FIGURE 1. Transient formation in a straight pipe initiated by sudden opening of a valve.

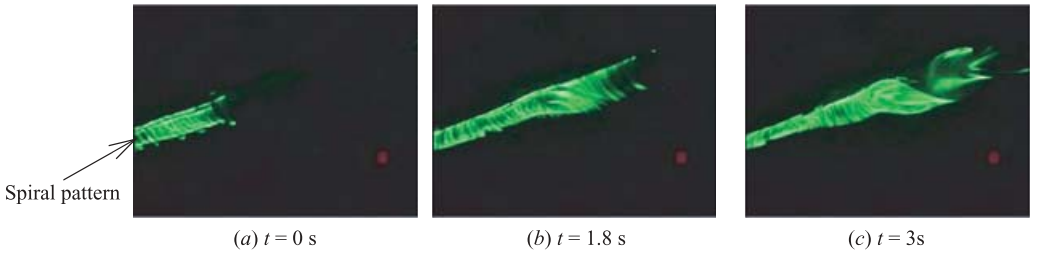

FIGURE 2. Transient formation over a delta wing caused by an increase in flow speed.

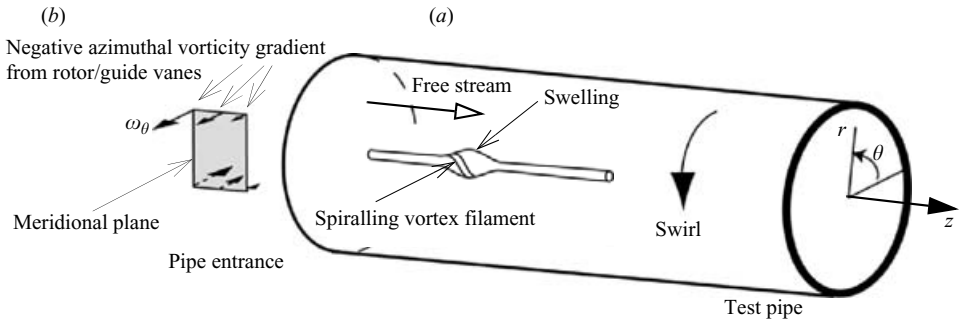

FIGURE 3. (*a*) A definition sketch and (*b*) the negative azimuthal vorticity gradient at the pipe entrance.

These spiralling vortex filaments, observed mostly in the steady condition, have been called various names such as vortex-ring structures (Escudier *et al.* 1982), striated vortices (Payne, Ng & Nelson 1988), and tassel vortices (Lowson 1988).

These dyed particles are drawn into the low-pressure centre of vortex filaments and become aligned approximately with the local vorticity vector. Therefore the spiralling pattern may be interpreted as an approximate manifestation of a spiralling vortex filament. The vorticity along the filament can be decomposed using the cylindrical coordinates of figure 3(*a*). The axial coordinate z is positive in the downstream direction; viewed from downstream, the azimuthal angle θ is taken to be positive counterclockwise, in the same direction as swirl imparted upstream.

Figure 3(*b*) shows, at the entrance to the test pipe, the azimuthal vorticity drawn on a meridional plane, whose magnitudes are shown to decrease in the downstream direction. This negative azimuthal vorticity gradient arises in the start-up.

To explain this concisely, it is easier to consider the following case that is slightly different from that of figure 1: the free-stream velocity remains constant and the vorticity, generated by a vorticity generator such as a rotor or stationary guide vanes located upstream of the test pipe, begins to increase in time (e.g. by an increase in rotor speed or guide vane opening). As the vorticity increases in time, so do its components, ω_z and ω_θ. Here we focus on the temporal increase in ω_θ. A fluid particle entering the pipe entrance possesses higher ω_θ than one which entered earlier; as these particles are carried by a constant free-stream velocity and flow into the pipe, the temporal increase in ω_θ appears as a spatial decrease in the downstream direction. This gives rise to the negative gradient of ω_θ in z: $\partial\omega_\theta/\partial z < 0$ shown in figure 3(*b*).

We offer our interpretation that the initial radial swelling and its subsequent growth are induced by this negative gradient of ω_θ. The azimuthal vorticity is coupled with ω_z, which changes in time and space, too. But for interpretation we only need consider $\partial w_\theta/\partial z$. As long as the axial gradient of the azimuthal vorticity remains negative, the radial expansion is induced. Thus, the sign of $\partial\omega_\theta/\partial z$, a generalization of the sign-switch in ω_θ (Brown & Lopez 1990), serves as a single descriptor for the radial change of a vortex core, from its inception to the steady state.

We will show this role of the azimuthal vorticity gradient in the radial deformation in two analyses: (*a*) a kinematic analysis in § 3 resulting in equation (2), where the gradient of ω_θ appears explicitly as a source term for u_r, followed by two examples in § 4, and (*b*) a dynamical analysis in § 5 leading to equation (13) where such a gradient is shown to be directly linked with the curvature change in the meridional streamline. In order to embody these analyses, details of the radial swelling and its growth are numerically simulated by the use of a modified vortex filament method (§ 6). The three-dimensional rendering of the results not only agrees favourably with the analyses but also enables us to track visually the evolutionary growth of a vortex breakdown.

Throughout this paper, we phrase our explanation strictly in the vocabulary of incompressible vortex dynamics where the pressure does not appear. This is because, unlike pressure, nowadays velocity and vorticity distributions can be globally mapped out by digital particle image velocimetry (DPIV). Hence, the present interpretation framed in terms of velocity and vorticity may be subjected to future DPIV testing.

We start from the kinematic induction of u_r by the azimuthal vorticity gradient.

3. A general relationship between radial velocity and the gradient of the azimuthal vorticity

A connection between the radial velocity, u_r, and the axial gradient of the azimuthal vorticity arises naturally once we eliminate the axial velocity u_z between the azimuthal component of vorticity,

$$\omega_\theta = \frac{\partial u_r}{\partial z} - \frac{\partial u_z}{\partial r},$$

and the equation of continuity for axisymmetric flows,

$$\frac{1}{r}\frac{\partial r u_r}{\partial r} + \frac{\partial u_z}{\partial z} = 0.$$

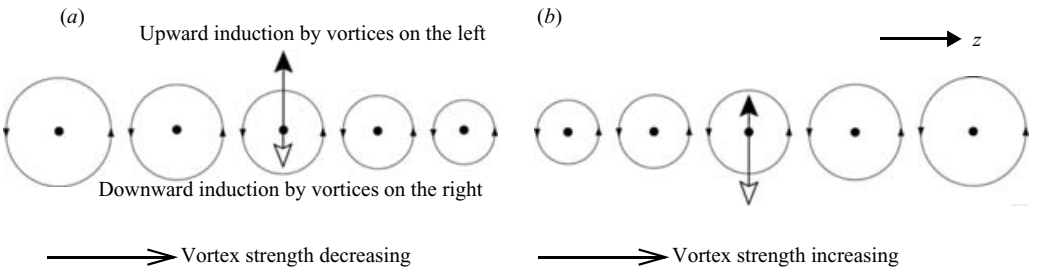

FIGURE 4. Induction by the neighbouring vortices. The vortices may be regarded as either two-dimensional or a head-on view of ω_θ of figure 3; (*a*) vortex strength decreasing from left to right, (*b*) vortex strength increasing.

This immediately results in a differential equation for u_r

$$\frac{\partial^2 u_r}{\partial r^2} + \frac{1}{r}\frac{\partial u_r}{\partial r} - \frac{u_r}{r^2} + \frac{\partial^2 u_r}{\partial z^2} = \frac{\partial \omega_\theta}{\partial z}, \tag{1}$$

where the axial gradient of the azimuthal vorticity $\partial\omega_\theta/\partial z$ appears as a non-homogeneous, source term for the radial velocity.

The effect of the vorticity gradient on u_r may be illustrated, in its most basic form, for a two-dimensional flow. Consider a single row of discrete vortices all of the same sign (figure 4), which may also be regarded as a head-on view of the azimuthal vorticity, ω_θ, of figure 3(*b*).

In figure 4(*a*) the strength of the vortices decreases from left to right, shown as circles with decreasing radii. If we focus upon the one in the middle, the downward induction by the neighbouring vortices on the right (hollow arrow) would be less than the upward induction by the neighbouring vortices on the left (filled arrow); as a net result, the middle vortex moves upward.

If the strength of the vortices increases from left to right, shown as circles with increasing radii (figure 4*b*), then the middle vortex would move downward. If all the vortices were of the same strength, the upward and downward inductions would be the same. No matter how strong the individual vortices are, there is no vertical movement. In other words, vertical motion occurs only when there is a change in the strength of vortices in relation to adjacent ones, i.e. the z-gradient of vorticity.

This can be seen analytically by solving equation (1) for unbounded flows. We apply the Hankel transform involving a kernel of $rJ_1(\alpha r)$ and obtain the following result (Appendix A):

$$u_r(r, z) = -\frac{1}{2\pi}\int_{-\infty}^{\infty} \mathrm{d}z' \int_0^{\infty} \frac{\partial \omega_\theta(r', z')}{\partial z'} \sqrt{\frac{r'}{r}}\, Q_{1/2}(\zeta)\, \mathrm{d}r', \tag{2}$$

where $Q_{1/2} = Q^0_{1/2}$ is the Legendre function of the second kind of the zeroth degree and of the order $1/2$, and

$$\zeta \equiv \frac{r^2 + r'^2 + (z - z')^2}{2rr'} \geqslant 1. \tag{3}$$

In obtaining (2), the following identity (Watson 1966) is used after the inverse Hankel transform:

$$\int_0^{\infty} \mathrm{e}^{-\alpha t} J_1(bt) J_1(ct)\, \mathrm{d}t = \frac{1}{\pi\sqrt{bc}} Q_{1/2}\left(\frac{\alpha^2 + b^2 + c^2}{2bc}\right). \tag{4}$$

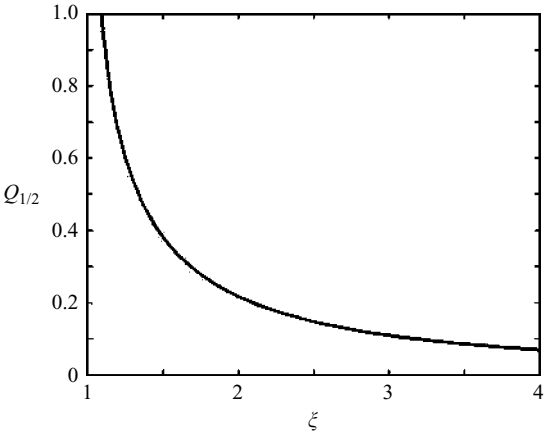

FIGURE 5. Plot of $Q_{1/2}$.

From the integral representation of $Q_{1/2}$ (Erdélyi 1953, p. 155)

$$Q_{1/2}(\zeta) = \int_0^\infty [\zeta + (\zeta^2 - 1)^{1/2} \cosh t]^{-3/2} \, \mathrm{d}t, \tag{5}$$

together with (3), it follows that $Q_{1/2}$ is always positive, as is also observed from figure 5. $Q_{1/2}$ has a singularity at $\zeta = 1$, corresponding to $r = r'$ and $z = z'$, the source point, as expected.

From this positive $Q_{1/2}$, a key conclusion follows immediately from (2): owing to a minus sign on the right-hand side, when the gradient of the azimuthal vorticity is negative everywhere, $\partial\omega_\theta/\partial z < 0$, then $u_r > 0$; the negative gradient of the azimuthal vorticity induces positive radial velocity or radial expansion, figure 4(*a*). Conversely, the positive gradient of the azimuthal vorticity induces negative radial velocity or radial contraction, figure 4(*b*). Further, due to the rapid decay of $Q_{1/2}$ away from the source point, the correspondence between the azimuthal vorticity gradient and radial change is expected to be local; this point will be confirmed by examples to be presented in § 4 and also by a numerical simulation in § 6.

In equation (2), the radial velocity at the observation point (r, z) at a given time is expressed as an integral carried over all sources, i.e. the gradients of the azimuthal vorticity. As such, it should be derived from the Biot-Savart law; this is shown in Appendix B. However, the derivation from the Biot-Savart law, with integrals involving vorticity rather than its gradient, required a sequence of steps, through which we were guided only by knowing this final result. Also, from the original form of the Biot-Savart formula, one cannot draw any conclusion about the sign of u_r directly. In contrast, the above direct derivation starting from a differential equation (1) and resulting in equation (2), where $\partial\omega_\theta/\partial z$ appears explicitly as a source term, seems to display naturally both the role of the axial gradient of the azimuthal vorticity and the complete dependence of the sign of u_r only on that of $\partial\omega_\theta/\partial z$. Furthermore, according to the present approach, it is trivial to extend these results to the asymmetric case by simply replacing u_r and $\partial\omega_\theta/\partial z$ with their azimuthally averaged values, e.g.

$$\bar{u}_r = \frac{1}{2\pi} \int_0^{2\pi} u_r \, \mathrm{d}\theta.$$

$Q_{1/2}$ in equation (2) may also be written in terms of the complete elliptic integrals of the first and second kind, respectively, as shown in equation (B 8) of Appendix B,

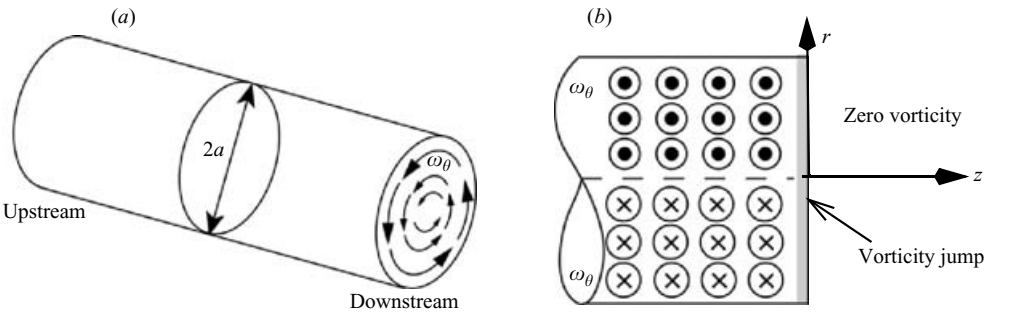

FIGURE 6. Definition sketch. (*a*) Perspective. Note circular arrows are the azimuthal vorticity and not swirl. (*b*) a meridional cut.

identical to those appearing in the expression for the streamfunction of a vortex ring, Lamb (1932).

A similar expression for the axial velocity u_z obtained by a rather cumbersome application of the Biot-Savart law is given in equation (B 18), Appendix B.

It is worthwhile to point out that these expressions for u_r and u_z are exact and general: they are valid in the presence of the other components of vorticity, ω_r and ω_z, and valid for both unsteady and steady flows, and even for viscous flows. For bounded flows, equation (1) can be solved subject to appropriate boundary conditions, but even when there is a surrounding pipe wall, equation (2) for u_r and the one for u_z in (B 18) are valid as long as the vortex centre remains at the centre of the pipe. This is because the effect of the wall can be replaced by the mirror image of the centre vortex, which is located at infinity.

4. Two examples

To exemplify a radial bulge induced by the azimuthal vorticity gradient, we apply the preceding general results to a particular case: a semi-infinite vortex core initially straight and having only an azimuthal vorticity component, ω_θ. This simple model of non-swirling flow serves to illustrate the key feature most conveniently. Since there is no axial component of vorticity, the flux of vorticity normal to any cross-section of the vortex is zero. Therefore, this vortex without circulation, can terminate in flow with its open end at $z=0$ (see figure 6). The vortex extends from $z=0$ to far upstream, $z=-\infty$. Outside of the core, $r>a$, $\omega_\theta=0$. Downstream of the open end, $z>0$, the vorticity is zero even for $r<a$; at $z=0$ there is a discontinuity in vorticity.

Inside the vortex, the azimuthal vorticity is continuously distributed. If discretized (figure 6*b*), this would correspond to an array of vortex rings occupying multiple annuli. For $t<0$, induction is off and our interest is focused at $t=0$ when the induction is turned on (e.g. 'solid barriers' separating the annuli dissolve). We will start with the simplest, example 1, where ω_θ is constant, and continue to example 2, where it varies in z.

Example 1: constant azimuthal vorticity

Upstream of the open end, $z<0$, the azimuthal vorticity is a constant, $\omega_{\theta 0}$. Thus the azimuthal vorticity is given by

$$\omega_\theta = \omega_{\theta 0}[1 - H(z)]H(a-r), \tag{6}$$

where $H(z)$ is a step function.

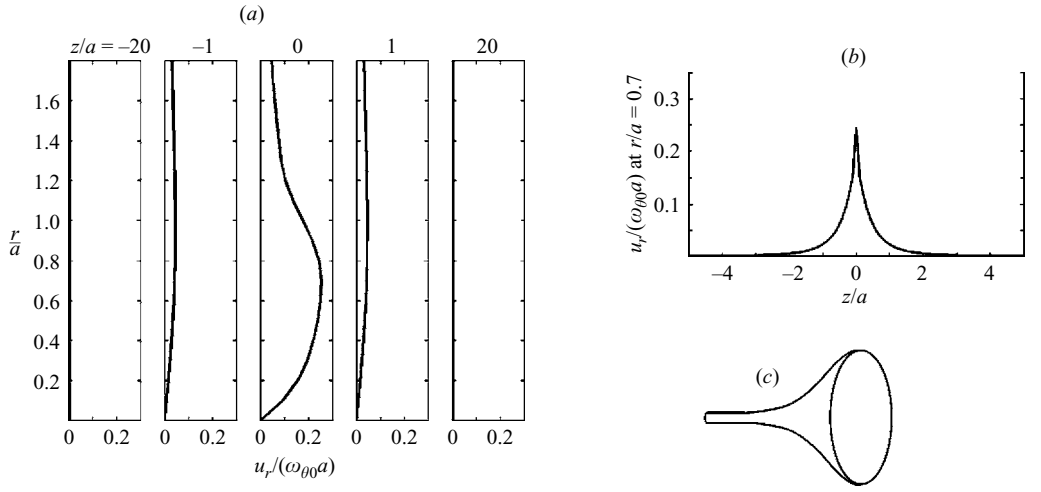

FIGURE 7. u_r for example 1: (*a*) radial velocity profile, (*b*) radial velocity vs. axial distance, (*c*) expansion of the open end.

The negative vorticity gradient exists only at the open end $z=0$, where the vorticity drops from $\omega_{\theta 0}$ to zero, in the form of a delta function:

$$\frac{\partial \omega_\theta}{\partial z} = -\omega_{\theta 0}\delta(z)H(a-r). \tag{7}$$

Note that although in the meridional representation, figure 6(*b*), the sense of the rotation of top and bottom vortices is opposite to each other, with regard to the respective azimuthal unit vectors pointing in the counterclockwise direction, figure 6(*a*), their signs are both positive. Thus for the bottom as well as for the top, the gradient of the azimuthal vorticity is negative at $z=0$.

Application of equation (2) yields

$$u_r(r,z) = \omega_{\theta 0} a F(r,z), \tag{8a}$$

where

$$F(r,z) = \frac{1}{2\pi a}\int_0^a \sqrt{\frac{r'}{r}}\, Q_{1/2}\left(\frac{r^2+r'^2+z^2}{2rr'}\right) \mathrm{d}r'. \tag{8b}$$

Figure 7(*a*) is the profile of radially induced velocity, u_r, at five axial locations, showing explicitly the radially outward velocity. Figure 7(*b*) shows a plot of u_r at $r/a=0.7$ versus z; u_r attains its maximum at $z=0$ and decays rapidly within an axial distance of the vortex core diameter. As a result, the open end of the vortex with the negative azimuthal vorticity starts to bulge while the rest remains virtually straight, figure 7(*c*).

Equation (B 18) in Appendix B is used for figure 8(*a*), the profile of axially induced velocity, u_z, at five axial locations, and figure 8(*b*), a plot of the axial velocity at the vortex centreline. The radial profiles of the axially induced velocity are jet-like and triangular, as expected from the constant $\omega_{\theta 0}$, and the deceleration occurs rapidly toward the open end of the vortex: the axial velocity at $z=0$ is half of that far upstream. As a consequence of the deceleration, fluid particles start to collect near the open end and we call their accumulation a *pile-up*. The radially outward velocity and the axial deceleration or the pile-up at $z=0$ are of course related by continuity; a defect in mass flux in the axial direction is balanced by radial outflow.

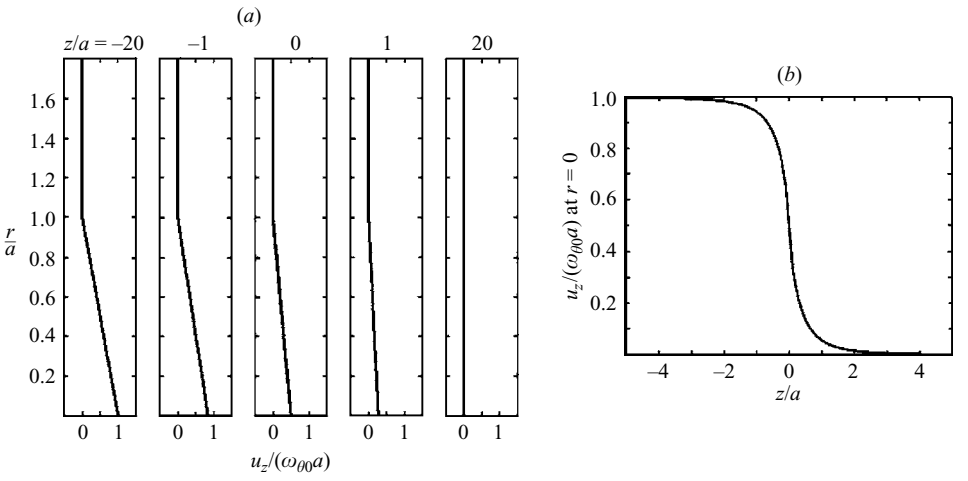

FIGURE 8. u_z for example 1: (*a*) axial velocity profile, (*b*) axial velocity vs. axial distance.

A referee brought to our attention the fact that this radial expansion and the axial pile-up is analogous to the magnetic field induced by electric current for an open-ended solenoid.

Example 2: varying azimuthal vorticity

We extend our consideration from a stepwise decrease in vorticity to a case where the azimuthal vorticity varies continuously in the axial direction but still remains unchanged radially, i.e., $\omega_\theta(z)H(a-r)$. Equation (2) becomes

$$u_r(r,z) = -a\int_{-\infty}^{0} \frac{\partial \omega_\theta(z')}{\partial z'} F(r, z-z')\,\mathrm{d}z'. \tag{9a}$$

where F is given in equation (8*b*).

When the azimuthal vorticity varies linearly in z between $-l < z < 0$, where $\omega_\theta = -(\omega_{\theta 0}\, z)/l$ and for $z < -l$, $\omega_\theta = \omega_{\theta 0}$ (see figure 9(*a*) where $l = a$), equation (9*a*) becomes

$$u_r(r,z) = \frac{\omega_{\theta 0}}{l} a \int_{z}^{z+l} F(r,\eta)\,\mathrm{d}\eta. \tag{9b}$$

Figure 9(*b*) shows u_r for $r = 0.7a$, indicating the radial expansion, figure 9(*c*). For future reference, we note that the radial swelling extends into the plateau region $z < -l$, where the azimuthal vorticity becomes constant. The fact that the radial velocity is positive even in such a plateau region may be seen explicitly by evaluating equation (9*b*) at $z = -l$; from the symmetry of F with respect to η,

$$u_r(r,-l) = \frac{\omega_{\theta 0}}{l} a \int_{0}^{l} F(r,\eta)\,\mathrm{d}\eta \tag{9c}$$

which is positive.

5. Dynamical relationship between the gradient of the azimuthal vorticity and the streamline curvature

Equation (2) in § 3 was derived by using only the equation of continuity and the definition of vorticity; therefore, as stated earlier, it is a kinematic relationship. As

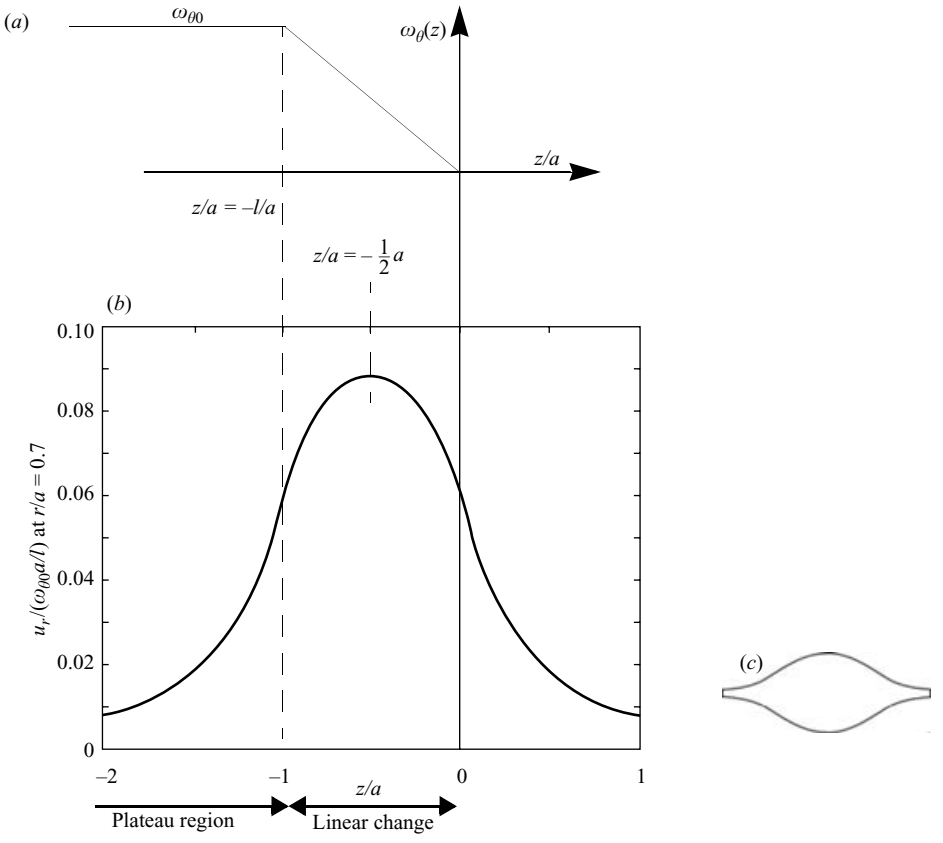

FIGURE 9. Example 2: (*a*) A linear change in the azimuthal vorticity ($l = a$), (*b*) radial velocity vs. axial distance, and (*c*) radial expansion.

a complement to this, we present, from the equation of motion in the meridional plane, a dynamical relationship between (i) the gradient of the azimuthal vorticity and (ii) the curvature of the instantaneous streamline.

In the meridional plane (r, z plane), we choose meridional streamline coordinates (s, n), where s is along, and n normal to, the cut of an instantaneous streamsurface by the meridional plane, called the meridional streamline (figure 10*a*).

From the axisymmetric and inviscid equations of motion written in this coordinate system, one can show exactly (equation (C 10) in appendix C) that

$$\frac{\partial \omega_\theta}{\partial s} = \frac{1}{r_m^2}\frac{\partial r_m}{\partial t} + \frac{\partial}{\partial s}\left(\frac{C}{4\pi^2 r^2 q_m}\frac{\partial C}{\partial n}\right) - \frac{\partial}{\partial s}\left(\frac{1}{q_m}\frac{\partial H}{\partial n}\right) \tag{10}$$

together with ((C 12) and (C 13))

$$\frac{\partial C}{\partial n} = 2\pi r\omega_s = 2\pi r\omega_m \cos\phi_m, \quad \frac{\partial C}{\partial s} = -2\pi r\omega_n = -2\pi r\omega_m \sin\phi_m. \tag{11}$$

Here, ω_θ is the azimuthal vorticity, r_m the radius of curvature of the meridional streamline, t the time, $q_m = \sqrt{u_r^2 + u_z^2}$ the meridional velocity, $C(r, z, t) = C(n, s, t) = 2\pi r u_\theta$ the local circulation, r the radial distance, $H = p/\rho + \boldsymbol{u}^2/2$ the total head, $\omega_m = \sqrt{\omega_r^2 + \omega_z^2}$ the meridional vorticity, ω_s and ω_n are vorticity components tangent and normal to the meridional streamline (figure 22, Appendix C), respectively, and

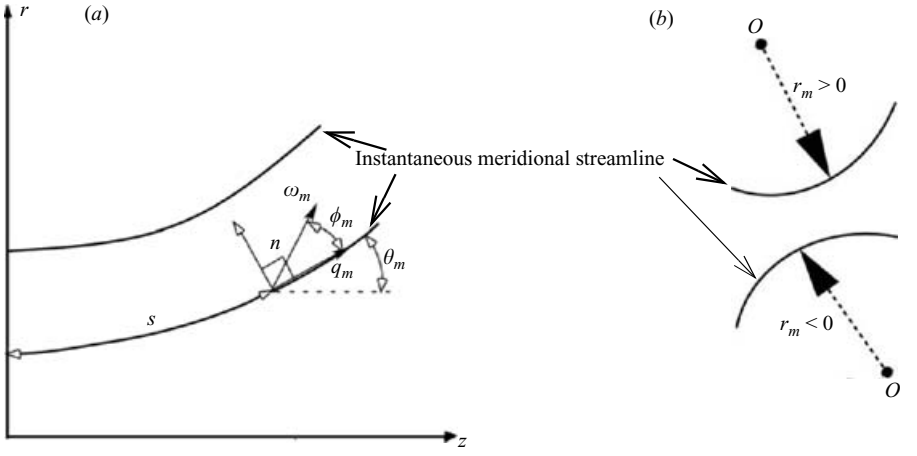

FIGURE 10. Streamlines in the meridional plane; (*a*) streamline coordinates, (*b*) sign-convention for the radius of curvature.

ϕ_m the angle between ω_m and q_m. The sign convention of the radius of curvature is shown in figure 10(*b*) together with its centre, O. This result is applicable both for confined and unconfined flows.

For the special case of the steady state where the first term on the right-hand side of equation (10) drops out, integration in s yields

$$\omega_\theta = \frac{C}{4\pi^2 r^2 q_m}\frac{\partial C}{\partial n} - \frac{1}{q_m}\frac{\partial H}{\partial n}. \tag{12}$$

When n is replaced with the stream function ψ by $\mathrm{d}n = \mathrm{d}\psi/rq_m$ (dropping a factor of 2π), this becomes the Bragg–Hawthorne (1950) equation, a starting point for many investigations of steady-state vortex breakdowns. When the circulation does not change along the streamsurface, $\partial C/\partial s = 0$, Brown & Lopez (1990) noted $\partial C/\partial\psi = \mathrm{d}C/\mathrm{d}\psi = \omega_z/u_z$, where ω_z and u_z are the axial component of vorticity and velocity, respectively. This may also be obtained from equations (11) as a special case of $\phi_m = 0$, i.e. the meridional vorticity being aligned with the meridional velocity.

From this, they transformed the Bragg–Hawthorne equation into an expression which most transparently reveals that, for a diverging streamsurface, a competition between the two terms on the right-hand side of equation (12) can result in the negative ω_θ, i.e. ω_θ sign-switch in a radially expanded region. The sign-switch has been confirmed by experiments (e.g. Shih & Ding 1996). It also points out the role of the total-head variation (originated far upstream such as within the boundary layers over the guide vanes and subsequently redistributed) in establishing a steady-state in an otherwise inviscid process. Still, such steady-state analysis, where the streamsurfaces diverging downstream are assumed to be already established, does not appear to explain why such radial expansion occurs in the first place.

We return to the present transient start-up when the circulation ramps up from zero to its steady-state value during a ramp-up time τ. When this inertial time scale, τ, is shorter than the slower viscous scale, the viscous term is not significant and the inviscid equation (10) is appropriate. Furthermore, for a fast ramp-up with a shorter τ, the second and third terms on the right-hand may become negligible at the start-up. More precisely, this is so when a dimensionless parameter involving τ, $B = (C_{\infty max}^2\tau)/(4\pi^2 r_c^3 U_\infty)$ is small, where $C_{\infty max}$ is the steady-state value of the total

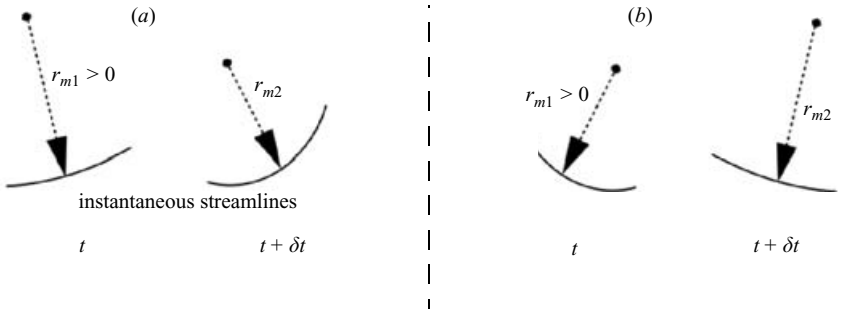

FIGURE 11. Curvature change and azimuthal vorticity gradient; (*a*) negative azimuthal vorticity gradient, (*b*) positive azimuthal vorticity gradient.

circulation $C_\infty(z, t) = \lim_{r\to\infty} 2\pi r u_\theta$, r_c the vortex core radius, and U_∞ the free-stream velocity. This parameter B arises after non-dimensionalizing each term of equation (10) by these characteristic parameters. For small values of B, equation (10) at start-up becomes

$$\frac{\partial \omega_\theta}{\partial s} \approx \frac{1}{r_m^2}\frac{\partial r_m}{\partial t}. \tag{13}$$

According to equation (13), both the change in the azimuthal vorticity along the meridional streamline, $\partial\omega_\theta/\partial s$, and the temporal change in the radius of curvature r_m have the same sign. Thus, as sketched in figure 11(*a*), once the radial expansion starts in the region where $\partial\omega_\theta/\partial s < \theta$ and $r_{m1} > 0$, then it continues so that the meridional streamlines become more curved with a smaller radius of curvature, $r_{m2} < r_{m1}$. Hence, in the presence of the azimuthal vorticity decreasing downstream, a slight swelling initiated by such a negative vorticity gradient will continue to enlarge radially; the negative vorticity gradient promotes and sustains its subsequent growth.

Conversely, once the radial flattening starts in the region where $\partial\omega_\theta/\partial s > 0$ and $r_{m1} > 0$ (figure 11*b*), it further becomes levelled so that the streamlines have the larger radius of curvature $r_{m2} > r_{m1}$.

As stated, equation (13) is valid for a small B and at start-up. Even for a small B, it would lose its validity at the later stage of transient formation, when t/τ is large, because of the aforementioned role of the total head at a steady state.

The validity of equation (13) has been investigated by Johnson (2004), which we summarize next. By a numerical simulation similar to the one in § 6, the left-hand side of equation (10) is compared with its right-hand side, using (*a*) only the first term, i.e. the same one as the right-hand side of equation (13), and (*b*) the first and second term (the third term involving the total head is not evaluated because in this simulation pressure does not appear explicitly). For $B = 0.37$ and $t/\tau = 60$, which are perhaps beyond their presumed limits of accuracy, (*a*) and (*b*) are found to show the correct trend with that of the left-hand side. As expected, (*b*) follows the left-hand side more closely than (*a*) but even for (*a*), its sign, the most relevant, generally agrees with the one on the left-hand side. This similarity in trend is also found for $B = 15$ and $t/\tau = 1.5$. Additionally, the change in the curvature of the instantaneous streamline as shown in figure 11 has been found to correspond to that of the more commonly visible streaklines such as the ones to appear in § 6.

As a special case, when θ_m of figure 10(*a*) is small, $\partial\omega_\theta/\partial s \sim \partial\omega_\theta/\partial z$. Hence in the above argument, $\partial\omega_\theta/\partial s$ may be replaced by $\partial\omega_\theta/\partial z$. Viewed in this way, the

examples worked out in § 4 may be regarded as a subset of this case when $r_{m1} = \infty$ initially, and $C = 0$.

6. A numerical simulation

To give a more tangible form to the above analyses, we numerically simulated the transient formation. Here we present a condensed description of the numerical method employed, and discuss the key results (for additional details, see Cain 2001; Srigroram 2001; Wimer 2003; Johnson 2004).

We wish to follow the evolution of the vorticity field, which may be best captured by the vortex filament method (Leonard 1985). It has an advantage of preserving the identity of vortex lines while tracking their self-induced evolution. The vortex lines move by the local velocity determined by the Biot-Savart law. (Although the inviscid vorticity equation is not solved directly, this transport would satisfy the equation, e.g. Whitham 1963.) The method does not explicitly invoke pressure gradient, another advantage consistent with the approach of this paper.

An application of the vortex filament method to the vortex breakdown was attempted by Nakamura, Leonard & Spalart (1983). While their basic formulation methodology is adaptable to the present need, major modifications to be described shortly must be introduced to meet our objectives of simulating a transient process.

The vortex filament method has drawbacks, however. When the vortex filaments are subjected to a high degree of stretching, remeshing is in general desirable to maintain sufficient resolution in discretization (Ashurst & Meiburg 1988). Since our objective is to capture the general trend and compare qualitative features with the analyses, rather than to simulate the flow field most accurately, remeshing is not incorporated. Another drawback of the vortex filament method is its inability to account for the reconnection of vortex lines by dissipation (Meiburg 1995). Although this would become a problem in simulating the fully steady state, for the present study limited to the evolutionary stage where the dissipative effect is expected to be small, the advantage of the vortex filament method is judged to outweigh this drawback. It is for these reasons that the vortex filament method is chosen.

6.1. *Description of simulation setup*

Simulation is restricted to axisymmetric vortex breakdown or a bubble in its formation stage in unconfined flow. The pipe entrance is at $z = 0$. This is also where all the actions of rotors and guide vanes in imparting swirl are concentrated within an infinitesimally thin disk, a concept known as the actuator-disk model in turbomachines (e.g. Greitzer, Tan & Graf 2004). In $z < 0$, the region upstream of rotors/guide vanes, flow is irrotational, convected with uniform free-stream velocity. Across $z = 0$, the fluid acquires circulation discontinuously. A vortex tube, with a prescribed circulation and its axis initially along z, materializes at $z = 0$ and flows into the region $z > 0$. The vortex tube is discretized as vortex filaments, which are closely packed both radially and circumferentially so that there is no empty space within the vortex tube. The total circulation around the vortex tube, which is prescribed at $z = 0$ and changes in time, is $C_\infty(t)$. It is radially distributed among the vortex filaments in such a way that the axial vorticity approximates that for a Burger vortex:

$$\omega_z = \frac{C_\infty(t)\exp(-(r/r_c)^2)}{\pi(r_c)^2}, \text{ corresponding to } u_\theta = \frac{C_\infty(t)}{2\pi r}[1 - \exp(-(r/r_c)^2)] \quad (14)$$

where r_c is the core radius taken to be 0.3 in terms of unit length.

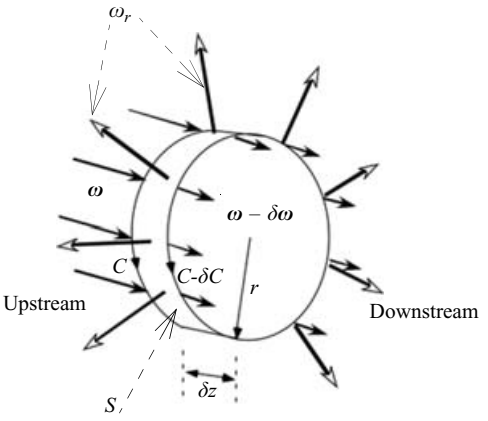

FIGURE 12. Efflux of radial vorticity due to a change in the circulation.

Each vortex filament is further discretized axially as smaller vortex segments, the end points of which are called nodes. In $z > 0$, self-induction among the nodes takes place, and they are advected downstream at a velocity equal to the sum of the induced velocity at each node and the free-stream velocity. The time-varying total circulation as well as local circulations distributed among vortex filaments remain unchanged as the nodes are advected downstream. As time progresses, vortex filaments keep emerging out of $z = 0$, and for $z > 0$, the circulation around the vortex tube displays a spatial variation decreasing downstream.

Whenever the total circulation changes, we need to ensure that the solenoidality condition for vorticity is satisfied: $\mathrm{div}\,\boldsymbol{\omega} = 0$. Consider a general case where the circulation changes (figure 12) and integrate the solenoidality condition over a cylindrical body, with radius r and axial length δz where the circulation decreases from C to $C - \delta C$.

Such a change in the circulation must be accompanied by the radial efflux of the vorticity emanating from the lateral surface S of the cylindrical body: $\mathrm{d}C/\mathrm{d}z = 2\pi r\omega_r$. Thus, there must be vortex filaments branching off radially and outwardly between two vorticity vectors, one entering the upstream circular surfaces of the cylindrical body, $\boldsymbol{\omega}$, and the other exiting downstream $\boldsymbol{\omega} - \delta\boldsymbol{\omega}$ (figure 12). The radial vorticity ω_r emanates from every point along the periphery of the surface S. Collectively it forms a vortex disk extending radially outward. (The presence of this vortex disk does not alter the analyses of §3–§5.) In the present simulation, the continuous radial disk is discretized into a finite number of radially branched filaments or spokes. This is the first and significant modification to Nakamura *et al.* (1983). Far downstream, there is no boundary condition specified, in contrast to Nakamura *et al.* where the vortex filaments assumed predetermined values. This is a second modification.

For changes in the circulation, we focus on the following: the total circulation prescribed at $z = 0$, $C_\infty(t)$, has a initially small value of 0.1 (in terms of unit length and time) in the forerunning period shown in blue, figure 13.

It then ramps up between $t = 0.6$ and $t = 0.8$ (corresponding to ramp-up time $\tau = 0.2$) in red, increasing to its final value, $C_{\infty max} = 20$. Thereafter it remains unchanged in the plateau, green. The free-stream velocity is always $U_\infty = 5$ (in terms of unit length and time). We define the circulation number based on the core radius, r_c, as $\Omega_{r_c} = C_{\infty max}/U_\infty r_c$. The final value, $C_{\infty max} = 20$, corresponds to $\Omega_{r_c} = 13.3$, which

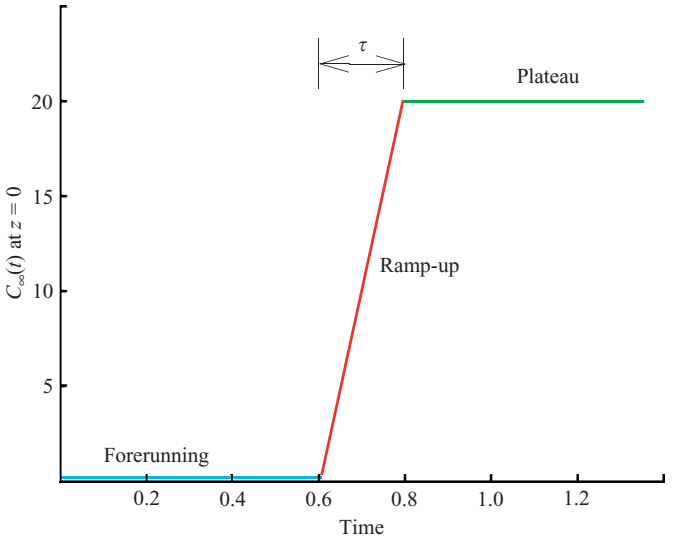

FIGURE 13. Temporal change of the circulation at $z = 0$.

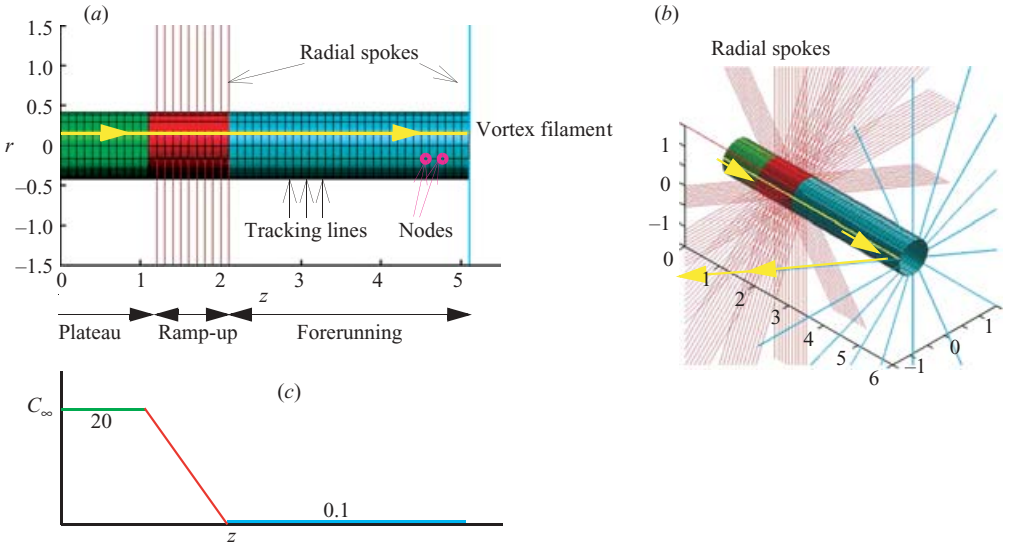

FIGURE 14. With induction off: (*a*) side view vortex filaments showing radial spokes and tracking lines, (*b*) perspective, and (*c*) spatial change in the circulation.

is in the range of steady-state values for pipe experiments: for instance, for a straight pipe (Kurosaka *et al.* 2003) $\Omega_{r_c} = 15$.

As the vortex tube is advected, this temporal change in the circulation specified at the actuator disk at $z = 0$, $C_\infty(z = 0, t)$, appears as a spatial variation along the vortex tube as $C_\infty(z, t)$. Figure 14 displays this in the same colour-code as figure 13 and is shown for the outermost filaments at $r = 0.42$, shaded like a solid cylindrical surface, in a side view, figure 14(*a*), and a perspective view, figure 14(*b*).

Although the induction always takes place in $z > 0$, before we present these inductive results we need to show the basic set-up in its simplest form. For this reason, the

induction is turned off in figure 14(a, b). Figure 14(c) shows the total circulation change along the vortex axis. The circulation decreases along the positive z-direction. The temporally increasing $C_\infty(z=0,t)$ at the pipe entrance, as it is advected in sequential order, manifests itself as decreasing from upstream to downstream. In figure 14(a, b), the lines that run axially along the length of the vortex tube are the vortex filaments, one of which is highlighted in yellow. Nodes, which discretize each vortex filament, emerge from $z=0$ in equal time-steps and are advected downstream with the same free-stream velocity. Hence, with the induction off, nodes are separated axially by equal distance and their radial positions remain unchanged, as shown. The circumferential lines are merely tracking lines connecting nodes of the vortex segments; they do not represent vorticity vectors. Once the induction is turned on, however, the velocity induced from the rest of the nodes determined by the Biot-Savart law would move each node to a new position. The radial positions of the nodes would change and the axial distances between them be no longer equal.

Shown also in figure 14(a, b) are radial spokes emanating from each node of the vortex filaments distributed circumferentially. Spokes emerge wherever the circulation changes, from the open end of the blue region, and all the nodes in the red region. These radial spokes are emitted from the vortex filaments at other radii but only those for the outermost radius are shown here. Radial spokes are also discretized in the radial direction and have their own nodes. Once the induction is turned on, these radial spokes would not remain straight; after they emerge at $z=0$ as straight lines, they would take the shape determined by the induction. Their complicated configurations, however, tend to conceal main features that we wish to emphasize. Therefore, these radial spokes, though present, will be suppressed hereafter in visualizing the results.

6.2. *Results*

For vortex filaments having the initial radial position, $r_i=0.12$, figure 15 shows subsequent evolution in perspective views. For all of them, a single filament is highlighted in yellow to display its twisting and turning. From $t=0$ to $t=0.6$, the forerunning blue region with the small total circulation of 0.1 emerges from $z=0$, the actuator disk.

When the ramp-up begins at $t=0.6$, the corresponding red region where the circulation changes linearly starts to emerge, as seen from the image at $t=0.65$. At $t=0.8$, when the circulation attains its final value of 20, a slight bulge takes shape and a vortex filament highlighted in yellow twists slightly; the green region with the constant value of $C_{\infty max}=20$ emerges immediately after. From $t=0.9$ to 1.0, the radial expansion grows, followed by the radial contraction downstream. Upstream of the red region, the radial expansion now propagates to the green region of constant circulation with additional twisting. At $t=1.35$ and 1.82, the green region diverges more radially and the downstream side of the red surface becomes recessed or caved-in, which implies a backflow. The entire evolutionary process is reminiscent of shock formation and for the t, z-plane representation of this, see Johnson (2004). The originally straight vortex core, after undergoing an initially modest bulge, changes into a shape bearing a resemblance to the observed bubble form of vortex breakdown, all being the result of self-induction. These images appear to compare well with figure 1(a–f). Next, we examine these results in detail.

6.3. *Initial generation of azimuthal vorticity gradient and swelling*

The initial twisting of the vortex filament observed at $t=0.8$ in figure 15 is an embodiment of the azimuthal vorticity gradient. The generating mechanism of azimuthal vorticity gradient near $z=0$ is shown schematically in figure 16, a view from the top. Consider the ramp-up region (red) where circulation increases in time. For vorticity

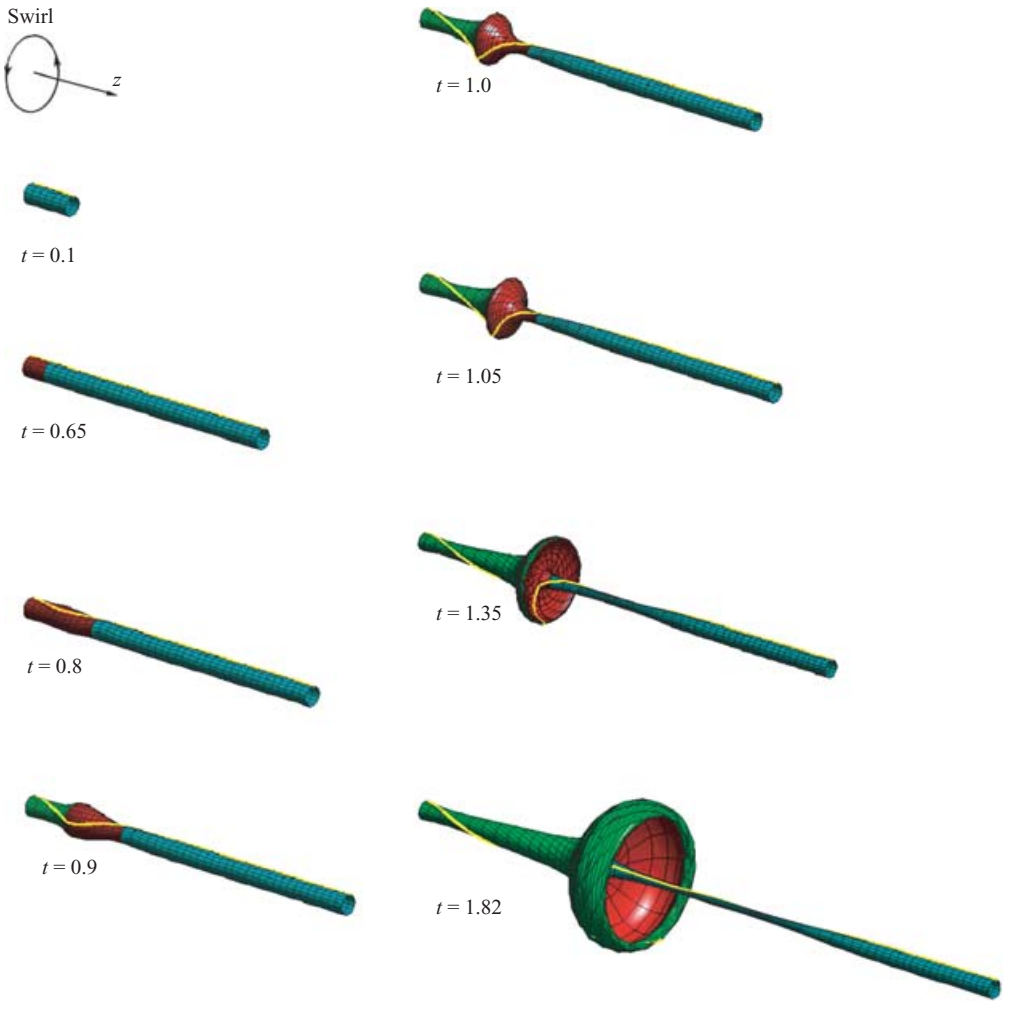

FIGURE 15. Temporal evolution in perspective; the same vortex filament is highlighted in yellow.

at $t = t_1$, its downstream end b is subject to azimuthal velocity determined by the circulation. Hence the end b spins circumferentially, while the node at its upstream end a at $z = 0$ is yet to spin. Therefore the vorticity a–b tilts in the circumferential direction, resulting in azimuthal vorticity $\omega_{\theta 1}$. At time $t = t_1 + \delta t$, new vorticity c–d emerges out of $z = 0$, as the vorticity a–b is swept downstream to a′ and b′. (For the reason described in § 6.4, ω_θ of a′–b′ becomes less than that of a–b, a difference which we ignore for now.) The downstream end d subject to higher circulation spins faster while the upstream end c at $z = 0$ has not yet spun. Hence vorticity c–d tilts more, resulting in larger azimuthal vorticity $\omega_{\theta 2} > \omega_{\theta 1}$: azimuthal vorticity decreases downstream. This is how in the ramp-up region the negative azimuthal vorticity gradient, $\partial \omega_\theta / \partial z < 0$, is generated, which causes radial swelling.

6.4. *Further comments on azimuthal vorticity*

In the ramp-up region, the circulation continuously decreases in the downstream direction. Hence, for any vorticity in the red region in figure 16 on its way downstream,

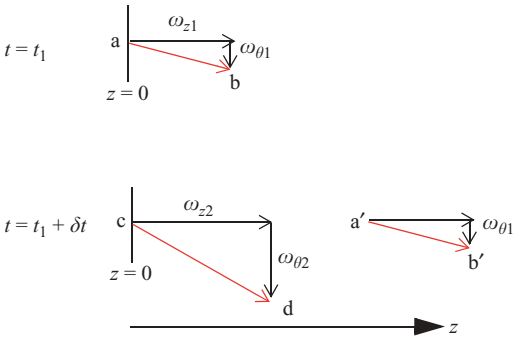

FIGURE 16. Generation of negative azimuthal vorticity gradient.

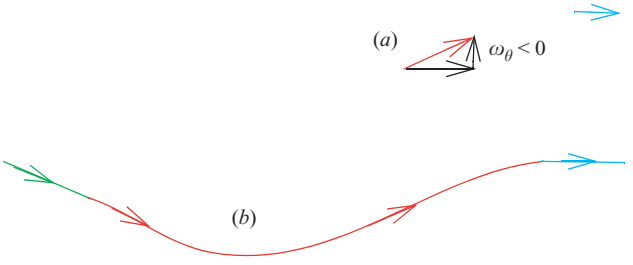

FIGURE 17. (*a*) Sign switch and vorticity in forerunning region, (*b*) twisting of a vortex filament.

its two ends continuously spin at different rates, the downstream end slower and the upstream faster. As a result of this differential rate of spin, the downstream end may eventually lag behind the upstream end, resulting in $\omega_\theta < 0$, a sign-switch in azimuthal vorticity in the ramp-up region, figure 17(*a*) red. On the other hand, in the forerunning region with a constant and small circulation, vorticity remains essentially axial, figure 17(*a*) blue. (Although at the open end of the forerunning region, there is a negative azimuthal vorticity gradient, it is too small to cause any perceptible effect.) Figure 17(*b*) is a composite of figures 16 and 17(*a*), schematically representings the vortex filament highlighted in yellow of figure 18(*a*), a computed result at $t = 0.82$. The decomposition of vorticity vectors along the yellow vortex filament is shown in white in figure 18(*a*).

In the red region of figure 18(*a*), the bulge attains its maximum near the middle, the point m, where the axial distance between tracking lines is the shortest. This embodies the connection between the radial expansion and the axial pile-up (§ 4, example 1).

Figure 18(*b*) shows the change of ω_θ along the yellow filament plotted against z. Figure 18(*c*) is the corresponding plot for its gradient. In the red region, from point p to point m and beyond, the azimuthal vorticity gradient is negative, which induces the radial expansion. Since near q, the vorticity is in the axial direction only, a change in ω_θ from negative to zero forces the generation of the positive azimuthal vorticity gradient near $z = 1$. There, this positive azimuthal vorticity gradient induces a slight contraction; a similar positive azimuthal vorticity gradient near $z = 0$ also induces a slight necking between $z = 0$ and point p.

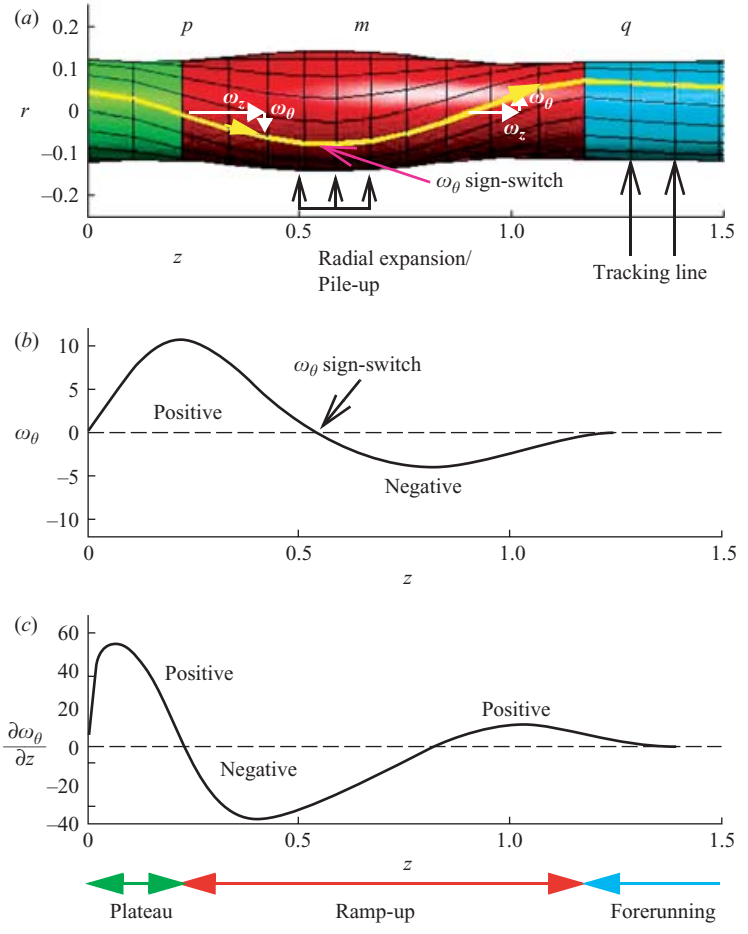

FIGURE 18. At $t = 0.82$; (*a*) side-view, (*b*) the azimuthal vorticity along the yellow vortex filament, and (*c*) azimuthal vorticity gradient.

6.5. *Plateau*

Figures 19(*a*) and 19(*b*) are enlarged views at $t = 1.35$, where the radial expansion and the pile-up appear exclusively in the green region of constant circulation. We call the rim of the recess a turning point where the vortex filament turns back. The concave recessed portion represents a backflow. Figure 19(*c*) shows the azimuthal vorticity distribution along the yellow vortex filament. The azimuthal vorticity sign-switch occurs in the radially divergent section.

From figure 19(*d*), the azimuthal vorticity gradient is negative in most of the green region, which corresponds to the radial expansion, as expected. Near the downstream end of the green region, a small portion with a positive azimuthal vorticity gradient induces the contraction of the streamsurfaces, thus providing a closure to the vortex breakdown. Therefore, the vorticity gradient is responsible both for the radial expansion and subsequent contraction, the latter imposing a limit to the radial growth of the vortex breakdowns.

The propagation of the radial expansion deep into the green plateau region of the steady-state circulation C_{max} is due to a differential rate of spin between the leading and trailing ends of a vorticity vector. As seen in example 2 of § 4, figure 9(*b*),

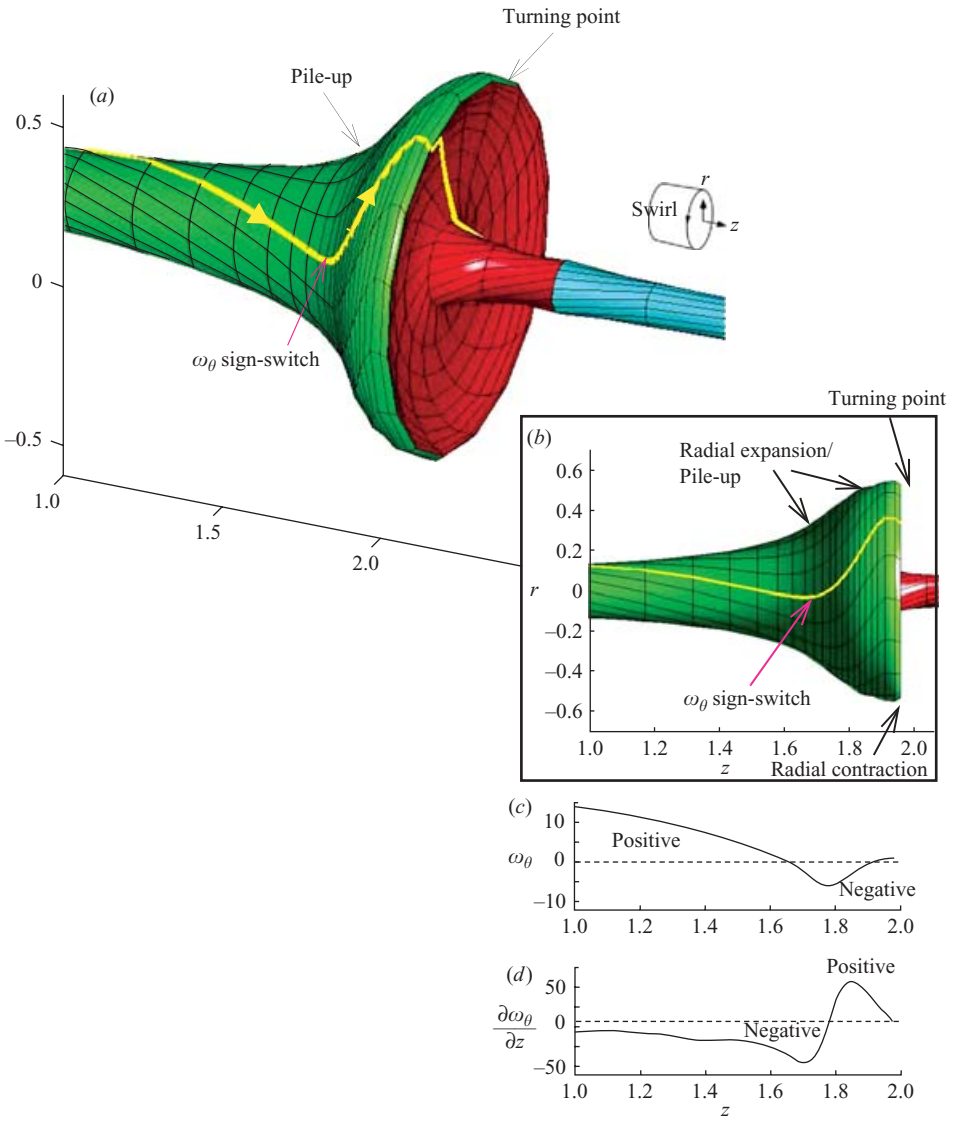

FIGURE 19. At $t = 1.35$; (*a*) perspective view, (*b*) side-view, (*c*) azimuthal vorticity along the yellow vortex filament, and (*d*) azimuthal vorticity gradient.

the radially outward expansion does not stop at the ramp-up region but extends somewhat beyond the downstream end of the plateau region. This extended expansion is illustrated in figure 20.

As a fluid particle located at a radius r is radially displaced outwards to $r + \delta r$, the leading end of a vorticity vector $\boldsymbol{\omega}$, b, also moves radially outwards. Since the circulation C_{max} remains the same, the azimuthal velocity at the point b positioned at a larger radius is less than that at a, the trailing end of $\boldsymbol{\omega}$: $u_{\theta b} < u_{\theta a}$. Due to this differential rate of spin, the azimuthal vorticity of $\boldsymbol{\omega}'$ is less than that of $\boldsymbol{\omega}$: $\omega'_\theta < \omega_\theta$. As a result, in the plateau region a negative azimuthal vorticity gradient is now set up, which induces radial enlargement there and provides a feedback to the farther upstream movement of the negative azimuthal vorticity gradient.

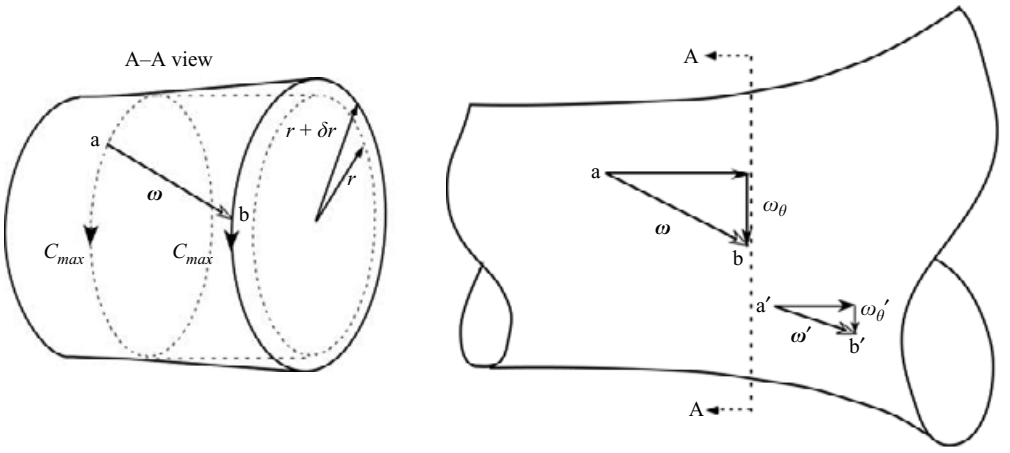

FIGURE 20. Tilting of a vorticity vector and the negative vorticity gradient in the plateau region.

The yellow vortex filament and its corresponding nodes emerge initially at a fixed location on the $z = 0$ plane. Thus, these nodes represent fluid particles released continuously at the same point. In other words, the yellow vortex filament consisting of such nodes can be interpreted as a streakline. Conversely, in flow visualization of vortex breakdowns, a dyed marker released from a fixed point is sucked into the low-pressure core of a vortex filament and stays there; therefore, as mentioned earlier, an observed streakline approximates a vortex filament. Hence we can associate the vortex filaments in the present numerical simulation with the dyed streaklines in flow visualization.

The visually misleading sense of rotation of the yellow streakline opposite to the upstream swirl has been a subject of controversy. The opposite-hand winding of the streakline is simply due to the continuous tilting of vorticity vectors in the azimuthal direction, from $\boldsymbol{\omega}$ to $\boldsymbol{\omega}'$ (figure 20) and beyond, caused by a difference in swirl between the smaller and larger radii. The pathlines still rotate in the same sense as the base swirl (Visbal 1996; Cain 2001). The opposite sense of rotation is another example of the familiar – but often ignored – deceptive nature of the streakline in unsteady flows (e.g. Kurosaka & Sundaram 1986).

The closeness of the outer and inner surfaces as observed in the image at $t = 1.82$ of figure 15 implies the proximity of opposing vorticity vectors and the resulting cross-vorticity diffusion. This and the steepening of vorticity gradient signify the need for viscosity in establishing steady-state.

For a bubble at such steady state, its downstream portion is known to change both azimuthally and periodically, which may be observable from figure 1(h). This disturbance is describable as $\exp[\mathrm{i}(m\theta - \Omega t)]$ where Ω is the frequency and m azimuthal wavenumber found to be $|m| = 1$ (Faler & Leibovich 1978; Garg & Leibovich 1979). Associated with this are emptying and filling of fluid in the bubble, occurring 180° apart in the azimuthal direction. However, before such asymmetry develops, for the symmetric bubble, there is filling from downstream, but no emptying, as seen from figure 1(f). This result from flow visualization is consistent with figure 19. (Numerical extension to a steady state including asymmetry and viscosity as well as experimental confirmation by DPIV of the relationship between negative azimuthal vorticity gradient and radial expansion is left to the future.)

7. Summary

We started by focusing on a simple but vexing question about the formative stage of axisymmetric vortex breakdown in a straight pipe: for an initially straight vortex core, what initiates its radial expansion in the first place? To answer this question, we presented our own interpretation within the framework of incompressible vortex dynamics without invoking pressure: it is the negative azimuthal vorticity gradient that triggers and self-sustains the radial expansion. By tracking a transient process, we argued that this negative azimuthal vorticity gradient emerges in a ramp-up region, then spreads into the plateau region having steady-state circulation.

Analytically, this role of the vorticity gradient specifically appears in two key equations: (2) and (13). Figure 4 best illustrates the basic physical element at work: it is the *relational* change of the azimuthal vorticity or its gradient, and not the magnitude of vorticity itself, that determines the net inductive effect of radial expansion.

The direct connection between the negative azimuthal vorticity gradient and the radial expansion are much in evidence in the three-dimensional rendering of the numerical simulation, figures 18 and 19. When the azimuthal vorticity gradient becomes positive, the expansion ends and radial contraction begins. Thus the azimuthal vorticity gradient acts as a driving force to start the initial swelling, spur subsequent expansion, and stop it.

C. B. C., J. D. W., W. F. J., and B. R. T. would like to express their gratitude for the US Air Force for support while at the University of Washington. M. K. acknowledges Dr Murray Tobak and Professor Ed Greitzer for their critical and constructive comments.

Appendix A

We apply the Hankel transform with a kernel of J_1, Bessel function of the first kind of the order 1, defined as

$$\bar{u}(\alpha) = \int_0^\infty r u_r J_1(\alpha r)\,\mathrm{d}r \tag{A 1}$$

which is related through its inverse

$$u_r = \int_0^\infty \alpha \bar{u}(\alpha) J_1(\alpha r)\,\mathrm{d}\alpha \tag{A 2}$$

to equation (1). By using

$$\int_0^\infty r\left(\frac{\partial^2 u_r}{\partial r^2} + \frac{1}{r}\frac{\partial u_r}{\partial r} - \frac{u_r}{r^2}\right) J_1(\alpha r)\,\mathrm{d}r = -\alpha^2 \bar{u}(\alpha),$$

we obtain

$$\frac{\mathrm{d}^2 \bar{u}(\alpha)}{\mathrm{d}r^2} - \alpha^2 \bar{u}(\alpha) = \bar{f}(\alpha) \tag{A 3}$$

where $\bar{f}$ is the Hankel transform fo the right-hand side of equation (1),

$$\bar{f}(\alpha) = \int_0^\infty r f J_1(\alpha r)\,\mathrm{d}r, \tag{A 4}$$

where $f = \partial\omega_\theta/\partial z$.

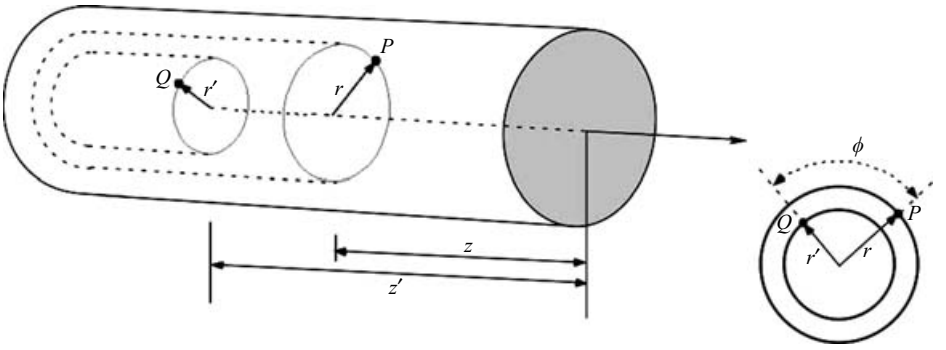

FIGURE 21. Source and observation points.

The solution of (A 3) is given by

$$\bar{u}(\alpha) = -\frac{1}{2\alpha}\int_z^\infty \bar{f}\exp[-\alpha(z'-z)]\,\mathrm{d}z' - \frac{1}{2\alpha}\int_{-\infty}^z \bar{f}\exp[-\alpha(z-z')]\,\mathrm{d}z'. \tag{A 5}$$

Taking inverse transform and substituting (A 4), we obtain

$$\begin{aligned} u_r = &-\frac{1}{2}\int_z^\infty \mathrm{d}z' \int_0^\infty r' f(r',z')\,\mathrm{d}r' \int_0^\infty J_1(\alpha r)J_1(\alpha r')\exp[-\alpha(z'-z)]\,\mathrm{d}\alpha \\ &-\frac{1}{2}\int_{-\infty}^z \mathrm{d}z' \int_0^\infty r' f(r',z')\,\mathrm{d}r' \int_0^\infty J_1(\alpha r)J_1(\alpha r')\exp[-\alpha(z-z')]\,\mathrm{d}\alpha \end{aligned} \tag{A 6}$$

Application of equation (4) yields equation (2).

Appendix B

For a vortex tube, we calculate the velocity at an observation point $P(r, z)$ induced by the vorticity at a source point $Q(r', z')$. The vorticity is independent of the polar angle.

B.1. *Radial velocity*

By applying the Biot-Savart law, the radial component of velocity at P, which is axisymmetric, is given by

$$u_r(r,z) = \frac{1}{4\pi}\int_0^\infty r'\,\mathrm{d}r' \int_{-\pi}^{\pi} I_r\,\mathrm{d}\phi, \tag{B 1}$$

where

$$I_r \equiv \int_{-\infty}^\infty \frac{\left[-\omega_\theta(r',z')(z'-z)\cos\phi - \frac{1}{2}\omega_z(r',z')r\sin 2\phi\right]\mathrm{d}z'}{(r'^2 - 2r'r\cos\phi + r^2 + (z'-z)^2)^{3/2}}, \tag{B 2}$$

and ϕ, the angle between P and Q, is shown in figure 21. When integrated over ϕ, the integral involving ω_z drops out and it becomes

$$I_r = -\int_{-\infty}^\infty \frac{\omega_\theta(r',z')(z'-z)\cos\phi\,\mathrm{d}z'}{(r'^2 - 2r'r\cos\phi + r^2 + (z'-z)^2)^{3/2}} \tag{B 3}$$

Integration by parts in z' yields

$$I_r = -\cos\phi \int_{-\infty}^\infty \frac{\partial\omega_\theta(r',z')}{\partial z'}\frac{\mathrm{d}z'}{\sqrt{r'^2 - 2r'r\cos\phi + r^2 + (z'-z)^2}}. \tag{B 4}$$

Thus

$$u_r(r,z) = -\frac{1}{2\pi_0}\int_0^\infty \sqrt{\frac{r'}{2r}}\,\mathrm{d}r' \int_{-\infty}^{\infty} \frac{\partial \omega_\theta(r',z')}{\partial z'} I_{r1}\,\mathrm{d}z', \tag{B 5}$$

where

$$I_{r1} = \int_0^\pi \frac{\cos\phi\,\mathrm{d}\phi}{\left[\dfrac{r'^2+r^2+(z'-z)^2}{2r'r} - \cos\phi\right]^{1/2}}. \tag{B 6}$$

In the following integral representation of Q_ν^μ (Erdélyi 1953, p. 156),

$$Q_\nu^\mu(\zeta) = \mathrm{e}^{\mu\pi\mathrm{i}}(2\pi)^{-1/2}(\zeta^2-1)^{\mu/2}\Gamma\left(\mu+\frac{1}{2}\right)\left[\int_0^\pi (\zeta-\cos t)^{-\mu-1/2}\cos\left(\left(\nu+\tfrac{1}{2}\right)t\right)\mathrm{d}t - C\right]$$

where $C = \cos(\nu\pi)\int_0^\infty (\zeta+\cosh t)^{-\mu-1/2}\,\mathrm{e}^{-(\nu+1/2)t}\,\mathrm{d}t$, by choosing $\mu = 0$ and $\nu = \frac{1}{2}$, we identify I_{r1} as

$$I_{r1} = \sqrt{2}\,Q_{1/2}\left(\frac{r'^2+r^2+(z'-z)^2}{2r'r}\right). \tag{B 7}$$

Substitution of (B 7) into (B 5) yields the same result as equation (2). One can express $Q_{1/2}$ in terms of the complete elliptic integrals by using the following identity (Abramowitz & Stegun 1970):

$$Q_{1/2}(\zeta) = \zeta\sqrt{\frac{2}{\zeta+1}}\,K\left(\sqrt{\frac{2}{\zeta+1}}\right) - [2(\zeta+1)]^{1/2}E\left(\sqrt{\frac{2}{\zeta+1}}\right). \tag{B 8}$$

B.2. *Axial velocity*

$$u_z(r,z) = \frac{1}{4\pi}\int_0^\infty r'\,\mathrm{d}r' \int_{-\pi}^{\pi} I_z\,\mathrm{d}\phi, \tag{B 9}$$

and I_z is defined as

$$I_z \equiv \int_{-\infty}^{\infty} \frac{[\omega_\theta(r',z')(r'-r\cos\phi) - \omega_r(r',z')r\sin\phi]\,\mathrm{d}z'}{(r'^2-2r'r\cos\phi+r^2+(z'-z)^2)^{3/2}}. \tag{B 10}$$

Integrated over ϕ, the integral involving ω_r drops out and integration by parts in z' yields

$$I_z = (r'-r\cos\phi)(I_1-I_2), \tag{B 11a}$$

where

$$I_1 = \frac{(\omega_\theta(r',z'\to\infty)+\omega_\theta(r',z'\to-\infty))}{(r'^2-2r'r\cos\phi+r^2)}, \tag{B 11b}$$

$$I_2 = \frac{1}{(r'^2-2r'r\cos\phi+r^2)}\int_{-\infty}^{\infty}\frac{\partial\omega_\theta(r',z')}{\partial z'}\frac{(z'-z)\,\mathrm{d}z'}{\sqrt{r'^2-2r'r\cos\phi+r^2+(z'-z)^2}}. \tag{B 11c}$$

Substitution of (B 11) into (B 9) yields

$$u_z(r,z) = \frac{1}{2\pi}\int_0^\infty [\omega_\theta(r',z'\to\infty)+\omega_\theta(r',z'\to-\infty)]r'I_{z0}\,\mathrm{d}r' - \frac{1}{2\pi}\int_0^\infty r'\,\mathrm{d}r'\int_{-\infty}^{\infty}\frac{\partial\omega_\theta(r',z')}{\partial z'}(z'-z)G\,\mathrm{d}z' \tag{B 12a}$$

where

$$I_{z0} \equiv \int_0^{\pi} \frac{(r' - r\cos\phi)}{(r'^2 - 2r'r\cos\phi + r^2)}\,\mathrm{d}\phi, \tag{B 12b}$$

and

$$G \equiv \int_0^{\pi} \frac{(r' - r\cos\phi)}{(r'^2 - 2r'r\cos\phi + r^2)\sqrt{r'^2 - 2r'r\cos\phi + r^2 + (z'-z)^2}}\,\mathrm{d}\phi. \tag{B 12c}$$

I_{z0} may be evaluated by contour integration as

$$I_{z0} = \frac{\pi}{r'} H(r' - r), \tag{B 13}$$

where H is a step function.

For G of (B 12*c*), upon making the following change in the integration variable:

$$\psi = \frac{\pi - \varphi}{2},$$

G may be written as

$$G = \frac{2}{(r'+r)\sqrt{(r'+r)^2 + (z'-z)^2}} \left[I_{z1}^{(1)} + \frac{2r(r'-r)}{(r'+r)^2} I_{z1}^{(2)} \right], \tag{B 14a}$$

where

$$I_{z1}^{(1)} \equiv \int_0^{\pi/2} \frac{\mathrm{d}\psi}{\sqrt{1 - \widehat{k}^2 \sin^2\psi}}, \tag{B 14b}$$

and

$$I_{z1}^{(2)} \equiv \int_0^{\pi/2} \frac{\sin^2\psi}{[1 - (1 - \widehat{k}'^2 \sin^2\widehat{\beta})\sin^2\psi]\sqrt{1 - \widehat{k}^2\sin^2\psi}}\,\mathrm{d}\psi, \tag{B 14c}$$

$$\left.\begin{aligned} \widehat{k}^2 &\equiv \frac{4r'r}{(r'+r)^2 + (z'-z)^2}, \quad \widehat{k}'^2 \equiv 1 - \widehat{k}^2 = \frac{(r'-r)^2 + (z'-z)^2}{(r'+r)^2 + (z'-z)^2}, \\ \sin\widehat{\beta} &\equiv \frac{|r'-r|}{(r'+r)} \sqrt{\frac{(r'+r)^2 + (z'-z)^2}{(r'-r)^2 + (z'-z)^2}}. \end{aligned}\right\} \tag{B 14d}$$

$I_{z1}^{(1)}$ of (B 14*b*) may be expressed in terms of the complete elliptic integral of the first kind, K, as

$$I_{z1}^{(1)} = K(\widehat{k}). \tag{B 15}$$

$I_{z1}^{(2)}$ of (B 14*c*) may be expressed (Gradshteyn & Ryzhik 1965)

$$I_{z1}^{(2)} = \frac{1}{\widehat{k}'^2 \sin\widehat{\beta}\cos\widehat{\beta}\sqrt{1 - \widehat{k}'^2\sin^2\widehat{\beta}}} \left[\frac{\pi}{2} - K(\widehat{k})E(\widehat{\beta}, \widehat{k}') - E(\widehat{k})F(\widehat{\beta}, \widehat{k}') + K(\widehat{k})F(\widehat{\beta}, \widehat{k}') \right], \tag{B 16}$$

where $K(\widehat{k})$ and $E(\widehat{k})$ are the complete elliptic integrals of the first and second kind, respectively: $F(\widehat{\beta}, \widehat{k}')$ and $E(\widehat{\beta}, \widehat{k}')$ are the incomplete elliptic integrals of the first and second kind, respectively. Substitution of (B 15) and (B 16) into (B 14*a*) yields

$$\begin{aligned} G = {} & \frac{2}{(r+r')\sqrt{(r+r')^2 + (z'-z)^2}} K(\widehat{k}) \\ & \pm \frac{1}{r'|z'-z|} \left[\frac{\pi}{2} - K(\widehat{k})E(\widehat{\beta}, \widehat{k}') - E(\widehat{k})F(\widehat{\beta}, \widehat{k}') + K(\widehat{k})F(\widehat{\beta}, \widehat{k}') \right] \end{aligned} \tag{B 17}$$

where for the $\pm$ sign, plus denotes $r' > r$, minus $r' < r$. Finally substitution of I_{z0} of (B 13) into (B 12a) yields

$$u_z = Z_1(r) - \frac{1}{2\pi} Z_2(r, z) \tag{B 18}$$

where

$$Z_1(r) = \int_{-\infty}^{\infty} \frac{[\omega_\theta(r', z' \to \infty) + \omega_\theta(r', z' \to -\infty)]}{2} \, \mathrm{d}r'$$

$$Z_2(r, z) = \int_0^{\infty} r' \, \mathrm{d}r' \int_{-\infty}^{\infty} \frac{\partial \omega_\theta(r', z')}{\partial z'} (z' - z) G \, \mathrm{d}z'.$$

Appendix C

We obtain the relationship between the gradient of azimuthal vorticity and the radius of curvature of the instantaneous streamsurface. For an instantaneous streamsurface cut by a meridional plane (r, z), introduce meridional streamline coordinates (s, n) where s is the distance along a meridional cut of the instantaneous streamsurface, to be called the meridional streamline, and n is normal to it. For any quantity, F,

$$\frac{\partial F}{\partial r} = \frac{\partial F}{\partial n} \cos\theta_m + \frac{\partial F}{\partial s} \sin\theta_m, \tag{C 1}$$

$$\frac{\partial F}{\partial z} = -\frac{\partial F}{\partial n} \sin\theta_m + \frac{\partial F}{\partial s} \cos\theta_m, \tag{C 2}$$

where θ_m is the angle between a tangent to the meridional streamline and the z-axis. The equation of continuity for axisymmetric flows may be written as

$$\frac{\partial (r q_m)}{\partial s} + r q_m \frac{\partial \theta_m}{\partial n} = 0, \tag{C 3}$$

where q_m is the meridional velocity (figure 10)

$$q_m = \sqrt{u_r^2 + u_z^2}. \tag{C 4}$$

We write the equation of motion as

$$\frac{\partial \boldsymbol{u}}{\partial t} + \operatorname{grad} H - \boldsymbol{u} \times \boldsymbol{\omega} = 0, \tag{C 5}$$

where H is the total head, $H = p/\rho + \frac{1}{2}\boldsymbol{u}^2$, and $\boldsymbol{\omega}$ the vorticity. The azimuthal component of the equation of motion may be expressed as

$$\frac{\partial C}{\partial t} + q_m \frac{\partial C}{\partial s} = 0, \tag{C 6}$$

where C is the local circulation, $C(s, n) = 2\pi r u_\theta$: of course, this is Kelvin's theorem. The radial and axial components of (C 5) are

$$\frac{\partial u_r}{\partial t} + \frac{\partial H}{\partial r} + \left[u_z \omega_\theta - \frac{u_\theta}{r} \frac{\partial (r u_\theta)}{\partial r} \right] = 0, \tag{C 7}$$

$$\frac{\partial u_z}{\partial t} + \frac{\partial H}{\partial z} + \left[-u_r \omega_\theta - \frac{u_\theta}{r} \frac{\partial (r u_\theta)}{\partial z} \right] = 0. \tag{C 8}$$

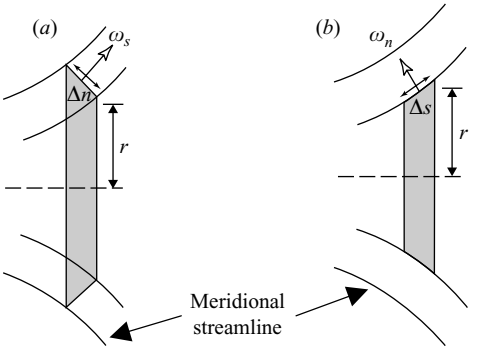

FIGURE 22. Integration volume.

Multiplying (C 7) and (C 8) by u_z and u_r, respectively, and subtracting, and by the use of (C 1) and (C 2), one obtains

$$\omega_\theta + \frac{\partial \theta_m}{\partial t} - \frac{C}{4\pi^2 r^2 q_m}\frac{\partial C}{\partial n} + \frac{1}{q_m}\frac{\partial H}{\partial n} = 0. \tag{C 9}$$

Differentiate (C 9) by s, one obtains

$$\frac{\partial \omega_\theta}{\partial s} - \frac{1}{r_m^2}\frac{\partial r_m}{\partial t} - \frac{\partial}{\partial s}\left[\frac{C}{4\pi^2 r^2 q_m}\frac{\partial C}{\partial n}\right] + \frac{\partial}{\partial s}\left[\frac{1}{q_m}\frac{\partial H}{\partial n}\right] = 0. \tag{C 10}$$

In deriving this, the following relationship is used: $\partial \theta_m / \partial s = 1/r_m$ where r_m is the radius of curvature of the instantaneous meridional streamline,

$$\frac{1}{r_m} = \frac{\mathrm{d}^2 r}{\mathrm{d}z^2}\left[1 + \left(\frac{\mathrm{d}r}{\mathrm{d}z}\right)^2\right]^{-3/2}. \tag{C 11}$$

For $\partial C/\partial n$ appearing in the third term of (C 10), apply the solenoidality condition for $\boldsymbol{\omega}$, $\operatorname{div} \boldsymbol{\omega} = 0$, to an integral over an elementary volume of a body of revolution with one side normal to the meridional streamline with length Δn, figure 22(a). This yields

$$\frac{\partial C}{\partial n} = 2\pi r \omega_s \tag{C 12}$$

where ω_s is the vorticity component tangent to the instantaneous streamline. Similar application of the solenoidality condition to another elementary volume of a body of revolution, figure 22(b), with a side surface of length Δs and tangent of the meridional streamline, yields

$$\frac{\partial C}{\partial s} = -2\pi r \omega_n. \tag{C 13}$$

REFERENCES

ABRAMOWITZ, M. & STEGUN, I. E. 1970 *Handbook of Mathematical Functions*, p. 337. Dover.
ASHURST, W. T. & MEIBURG, E. 1988 *J. Fluid Mech.* **189**, 87–116.
BELLAMI-KNIGHTS, P. G. 1976 *Trans. ASME: J. Fluids Engng* **98**, 322–323.
BENJAMIN, T. B. 1962 *J. Fluid Mech.* **14**, 593–629.
BERAN, P. S. & CULICK, F. E. C. 1992 *J. Fluid Mech.* **242**, 491–527.
BRAGG, S. L. & HAWTHORNE, W. R. 1950 *J. Aero. Sci.* **17**, 243–249.
BROWN, G. L. & LOPEZ, J. M. 1990 *J. Fluid Mech.* **221**, 553–576.

Buntine, J. D. & Saffman, P. G. 1995 *Proc. R. Soc. Lond.* A **449**, 139–153.

Cain, C. B. 2001 The self-induction theory of vortex breakdown. Master's Thesis, Department of Aeronautics and Astronautics, University of Washington. www.stormingmedia.us/48/4829/A482993.html.

Darmofal, D. L., Khan, R., Greitzer, E. M. & Tan, C. S. 2001 *J. Fluid Mech.* **449**, 61–84.

Delery, J. M. 1994 *Prog. Aerospace Sci.* **30**, 1–59.

Erdélyi, A. (Ed.) 1953 *Higher Transcendental Functions*, vol. 1. McGraw Hill.

Escudier, M. P., Bornstein, J. & Maxworthy, T. 1982 *Proc. R. Soc. Lond.* A **382**, 335–360.

Faler, J. H. & Leibovich, S. 1978 *J. Fluid Mech.* **86**, 313–335.

Garg, A. K. & Leibovich, S. 1979 *Phys. Fluids* **22**, 2053–2064.

Goldshtik, M. & Hussain, F. 1997 *Phys. Fluids* **9**, 263–265.

Grabowski, W. J. & Berger, S. A. 1976 *J. Fluid Mech.* **75**, 525–544.

Gradshteyn, Y. V. & Ryzhik, I. M. 1965 *Tables of Integrals, Series, and Products*, p. 388. Academic.

Greitzer, E. M., Tan, C. S. & Graf, M. B. 2004 *Internal Flow-Concepts and Applications.* Cambridge University Press.

Johnson, W. F. 2004 A comprehensive study of vortex breakdown flow mechanisms: computational investigation and preliminary control. Master's Thesis, Department of Aeronautics and Astronautics, University of Washington. www.stormingmedia.us/10/1074/A107424.html.

Kurosaka, M., Kikuchi, M., Hirano, K., Yuge, T. & Inoue, H. 2003 *Exps. Fluids* **34**, 77–86. For corrigendum, see www.miyazaki-u.ac.jp/∼kikuchi/Experiments_in_Fluids03/corrigendum.pdf

Kurosaka, M. & Sundaram, P. 1986 *Phys. Fluids* **29**, 3474–3477.

Lamb, H. 1932 *Hydrodynamics* p. 237, Dover.

Leibovich, S. 1984 *AIAA J.* **22**, 1192–1206.

Leibovich, S. & Kribus, A. 1990 *J. Fluid Mech.* **216**, 459–504.

Leonard, A. 1985 *Ann. Rev Fluid Mech.* **17**, 523–529.

Lowson, M. V. 1988 *AGARD CP*-438, paper 11.

Lucca-Negro, O. & O'Doherty, T. 2001 *Prog. Energy Combust. Sci.* **27**, 431–481.

Maxworthy, T., Hopfinger, E. J. & Redekopp, L. G. 1985 *J. Fluid Mech.* **151**, 141–163.

Meiburg, E. 1995 Chapter XV in *Fluid Vortices*, p. 659 (ed. S. I. Green). Kluwer.

Nakamura, Y., Leonard, A. & Spalart, P. R. 1983 *AGARD CP*-342, 27.1–27.13.

Payne, F. M., Ng, T. T. & Nelson, R. C. 1988 *AIAA J.* **26**, 137–143.

Ruith, M. R., Chen, P., Meiburg, E. & Maxworthy, T. 2003 *J. Fluid Mech.* **486**, 331–378.

Saghbini, J. C. C. & Ghoniem, A. F. 1997 *AIAA Paper* 97-0507.

Sarpkaya, T. 1971 *J. Fluid Mech.* **45**, 545–559.

Shih, C. & Ding, Z. 1996 *AIAA Paper* 96-0664.

Spall, R. E., Gatski, T. B. & Ash, R. L. 1990 *Proc. R. Soc. Lond.* A **429**, 613–637.

Srigrarom, S. 2001 On the formation of vortex breakdown over delta wings. PhD Thesis, Department of Aeronautics and Astronautics, University of Washington.

Srigrarom, S. & Kurosaka, M. 2000 *AIAA J.* **38**, 183–185.

Visbal, M. R. 1996 *AIAA Paper* 96-2074.

Wang, S. & Rusak, Z. 1997 *J. Fluid Mech.* **340**, 177–223.

Watson, G. N. 1966 *A Treatise on the Theory of Bessel Functions*, p. 389. Cambridge University Press.

Whitham, G. B. 1963 Chapter III in *Laminar Boundary Layers*, p. 122. Oxford University Press.

Wimer, J. D. 2003 A digital particle image velocimetry investigation of delta wing vortex flow and vortex breakdown. Master's Thesis, Department of Aeronautics and Astronautics, University of Washington. www.stormingmedia.us/80/8034/A803414.html.